A Novel Approach of Fabricating Monodispersed Spherical MoSiBTiC Particles for Additive Manufacturing

Zhenxing Zhou
Department of Materials Processing, Graduate School of Engineering, Tohoku University
Suxia Guo
Department of Materials Processing, Graduate School of Engineering, Tohoku University
Weiwei Zhou
Department of Materials Processing, Graduate School of Engineering, Tohoku University
Naoyoki Nomura (nnomura@tohoku.ac.jp)
Department of Materials Processing, Graduate School of Engineering, Tohoku University

Research Article

Keywords: Freeze-Dry Pulsated Orifice Ejection Method, MoSiBTiC alloy, Laser Powder Bed Fusion, Slurry

Posted Date: May 28th, 2021

DOI: https://doi.org/10.21203/rs.3.rs-540781/v1

Version of Record: A version of this preprint was published at Scientific Reports on August 16th, 2021.
See the published version at https://doi.org/10.1038/s41598-021-96187-w.

A Novel Approach of Fabricating Monodispersed Spherical MoSiBTiC Particles for Additive Manufacturing

Zhenxing Zhou, Suxia Guo, Weiwei Zhou* & Naoyoki Nomura*

Department of Materials Processing, Graduate School of Engineering, Tohoku University, Sendai, Miyagi, 980-8579, Japan

Abstract

It is very challenging to fabricate spherical refractory material powders for additive manufacturing (AM) because of their high melting points and complex compositions. In this study, a novel technique, freeze-dry pulsated orifice ejection method (FD-POEM), was developed to fabricate spherical MoSiBTiC particles without a melting process. Elemental nanopowders were dispersed in water to prepare a high-concentration slurry, which was subsequently extruded from an orifice by diaphragm vibration and frozen instantly in liquid nitrogen. After a freeze-drying process, spherical composite particles with arbitrary composition ratios were obtained. The FD-POEM particles had a narrow size range and uniform elemental distribution. Mesh structures were formed within the FD-POEM particles, which was attributed to the sublimation of ice crystals. Furthermore, owing to their spherical morphology, the FD-POEM particles had a low avalanche angle of 42.6°, exhibiting good flowability. Consequently, the combination of FD-POEM and additive manufacturing has great potential for developing complex refractory components used in industrial applications.

Keywords

Freeze-Dry Pulsated Orifice Ejection Method; MoSiBTiC alloy; Laser Powder Bed Fusion; Slurry

1 Introduction

Metallic alloys with superior mechanical and functional properties at elevated temperatures are in high demand in the aerospace industry [1,2]. Much attention has been paid to refractory intermetallic compounds in academic and industrial fields [3]. Mo–Si–B–based alloys are considered attractive candidates for use as structural materials in ultra-high-temperature applications [4,5], owing to their high melting points and superior high-temperature strength [4-14]. However, it is difficult to manufacture refractory components with complex internal or external structures using traditional methods. Therefore, additive manufacturing (AM) is being considered as a possible alternative [14].

Laser powder bed fusion (L-PBF) is a newly developed AM technique [15,16]. It utilizes a high-energy laser beam to selectively melt metallic powders to build three-dimensional objects in a layer-by-layer model [17]. Many factors influence the quality of the L-PBF fabricated parts. Among them, the properties of powders, such as their shape, size distribution, surface morphology, flowability, composition, and laser absorptivity, play a significant role. They directly influence the state of the melting pools, thereby affecting the quality of the final parts[14,18-24]. Presently, the powders, including Ti-, Fe-, Al- and Co-alloys, used for L-PBF, are mostly fabricated by mechanical milling, gas atomization (GA), plasma atomization (PA), plasma rotating electrode process (PREP), and plasma spheroidization (PS) [17,25-27]. However, each of these methods has significant limitations in the preparation of refractory alloy powders. For instance, powders produced by mechanical milling always have some shortcomings, such as irregular shape, poor flowability, uncontrolled particle size, or contamination [28]. Zhou et al. fabricated MoSiBTiC powders for L-PBF via high-energy ball milling and sieving [14,29]. Although the powder size of ~10-45 μm was controlled, abundant internal defects such as cracks were formed in the L-PBF builds, possibly owing to

poor flowability of powders and severe contamination. In contrast, GA and PA methods have been widely applied for spherical powder fabrication. Typical particle sizes of GA and PA powders range from 10 to 300 μm [30]. These particles are further sieved to obtain a more narrow distribution. Unfortunately, these methods have limited powder yield, and are time and energy consuming. Moreover, satellites and internal voids are usually present in GA and PA powders, which are detrimental to powder flowability and powder bed density during L-PBF [31]. In this regard, PREP has been highly recommended for obtaining spherical powders with decreased satellites and internal voids. However, owing to its high energy consumption and low powder yield, PREP is difficult to use for mass powder production [32-34]. Moreover, PS is a new technique that can be used for refractory powder fabrication [35,36]. The experimental results from Higashi et al. [36] showed that the PS MoSiBTiC alloy powders had a spherical shape similar to the atomized ones, while the content of elemental Ti or Si was significantly reduced owing to the ultra-high-temperature exposure. Notably, the GA, PA, PREP, and PS techniques require high-quality feedstock materials, such as wires, rods, or hydride alloy powders, further increasing the processing cost.

Therefore, in order to extend the application of L-PBF to refractory alloys, it is particularly important to develop an innovative approach for powder preparation to realize a spherical shape and stable elemental composition along with high yielding and low cost. In this study, a novel technique, the freeze-dry pulsated orifice ejection method (FD-POEM), was designed to fabricate monodispersed spherical refractory particles. The working mechanism of FD-POEM, the feasibility of fabricating a high-concentration slurry, and the characteristics of the FD-POEM particles were thoroughly investigated.

2 Experimental

2.1 Principle and Experimental Procedures of FD-POEM

The FD-POEM process involves several steps as follows: (a) slurry preparation (Fig. 1a). Mo, Si, MoB, and TiC submicron powders were selected as elemental materials and weighed according to the nominal atomic composition of 65Mo-5Si-10B-10Ti-10C (at. %) alloy. These powders were mixed in a certain amount of deionized water to form a uniform slurry with a concentration of X vol.% through combination of mechanical blending and ultrasonication at 273 K for 1 h. Here, X vol.% was defined as the volume fraction of powders in the slurry. (b) Pulsed-orifice ejection process (Fig. 1b). The slurry was dropped into liquid nitrogen driven by a pulsated orifice ejection apparatus, which included a pulsated orifice ejection body, diaphragm, and orifice pipe. A diaphragm was used to separate the droplets from the orifice pipe. The outer and inner diameters of the orifice pipe are 1.0 mm and 0.6 mm, respectively. The droplets were extruded from the orifice under diaphragm vibration using a pulse with a frequency of 10 Hz, followed by a square waveform. Owing to the surface tension, the extruded droplets became spherical and then froze instantly when dropped in the liquid nitrogen. (c) Freeze drying process (Fig. 1c). Monodispersed spherical particles were obtained via complete freeze-drying for more than 24 h.

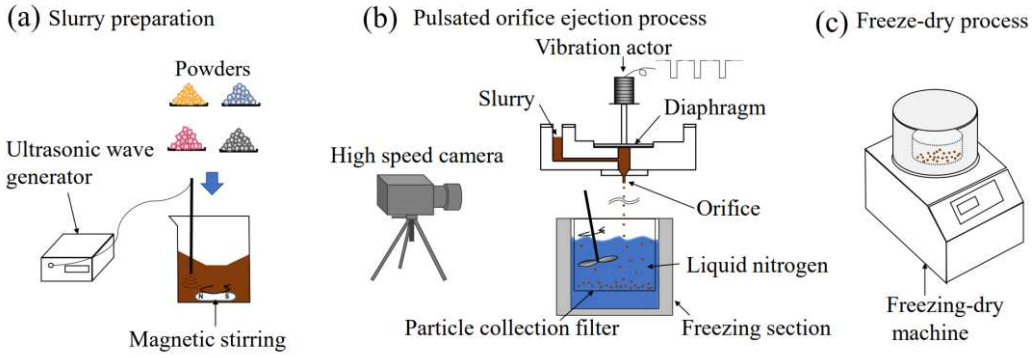

Figure 1. Schematic diagram of FD-POEM process: (a) Fabrication process of the slurry; (b) Preparation of composite particles by pulsated orifice ejection method; (c) Freeze-drying process.

2.2 Characterization

The zeta potential, of the slurries was measured using a zeta potential analyzer (SZ-100, HORIBA, Ltd., JP). The viscosity of the slurries was evaluated using a viscosity meter (DV2T VISCOMETER, AMETEK BROOKFIELD., US). Detailed images of the droplet ejection sequence were obtained using a high-speed camera (FASTCAM Mini UX100 type 800 K-M-8G, PHOTRON, INC., JP) with a frame rate of 4000/s and a shutter rate of 160000/s. The particle size and distribution of the FD-POEM particles were determined using an image analyzer connected to an optical microscope. The morphologies and elemental distributions of the FD-POEM particles were evaluated using a scanning electron microscope (SEM) (JSM-6010LV, JEOL, JP). The internal structure of the particles was observed using computer tomography (CT) that combined a series of X-ray images taken from different angles around the particles to create cross-sectional images (TUX-3200N, MARS TOHKEN SOLUTION Co. Ltd., JP). The powder flowability was characterized using the revolution method (Revolution Powder Analyzer, Mercury Scientific Inc. JP).

3 Result and Discussion

3.1 Fabrication of Uniform Slurry

The features of the raw materials are deemed to be important for FD-POEM. Fig. 2 shows the morphology of the raw powders. It is noted that the particle morphologies and sizes of the raw powders differ greatly, such as polyhedral-shaped Mo and TiC powders (Fig. 2a and d), lamellar-shaped Si powder (Fig. 2b), and irregularly shaped MoB powder (Fig. 2c). According to SEM observations, the particle sizes, d_{50}, of Mo, Si, MoB, and TiC powders were determined to be ~1.0, 4.3, 0.57, and 0.67 μm, respectively.

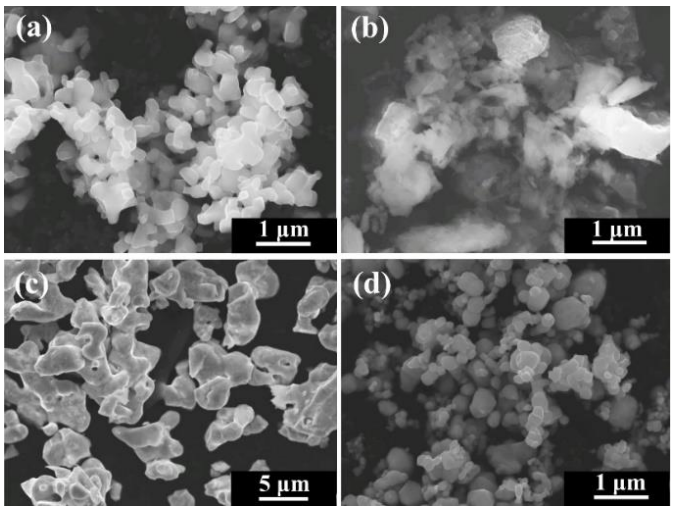

Figure 2. SEM images of the raw (a) Mo, (b)Si, (c) MoB, and (d)TiC powders.

Single-component slurries of raw Mo, Si, MoB, and TiC powders with a concentration of 5 vol.% were prepared separately. Figs. 3(a-d) show the appearance of different single-component slurries. Each slurry had a uniform color without obvious delamination, indicating that the raw powders were well dispersed in water. For comparison, the binary components of Mo-Si and multi-components of Mo-Si-MoB-TiC slurries were also prepared. As shown in Figs. 3(e) and (f), the mixed slurries maintained good dispersion, and the dispersion state did not change with an increase in the amount of the slurry components.

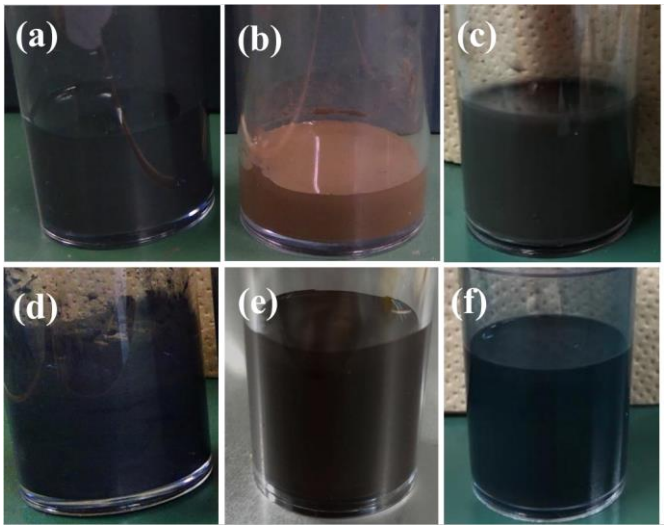

Figure 3. The appearance of 5 vol. % (a) Mo, (b) Si, (c)MoB, (d)TiC, (e)Mo-Si, (f)Mo-Si-MoB-TiC slurries.

To investigate the stability mechanism of the fabricated slurries several theoretical values that describe the particle motion in water were calculated. The ratio of d (Brownian motion distance)/ ν (sinking velocity) is often applied to characterize the nanopowder stability in slurries. A large d / ν

value means stable dispersion. In general, the particles can exist stably in water as the value of d / ν is larger than 20 [37-39]. The sinking velocity of particles follows the Stokes' law equation as [40],

$$\nu = \frac{2r^2(\rho - \rho_0)}{9\eta} \quad (1)$$

where ν is the velocity of sinking; r is the diameter of particle; ρ is the density of the particle; ρ_0 is density of the solution, and η is the viscosity of the solution. The Brownian motion of powders is calculated according to the Fluctuation-dissipation theorem [40],

$$d = \sqrt{2Dt} \quad (2)$$

where t is the time, d is the moving distance of the particle, and D is the diffusion coefficient. The diffusion coefficient D is expressed as

$$D = \frac{kT}{6\pi\eta r} \quad (3),$$

where k is the Boltzmann constant ($1.38064852 \times 10^{-23}$ J/K [40]); T is the temperature; η is the solution viscosity, and r is the particle radius. Correspondingly, the d / ν values are displayed in Table 1. It indicates that the slurries of Si and TiC are stable in view of the higher value of d / ν. However, the relative lower d / ν values suggested that the Mo and MoB powders are prone to sink; obviously, this is not consistent with the experimental results shown in Fig. 3.

Table 1 The Basic Parameters of Each Slurry.

	Mo	**Si**	**MoB**	**TiC**
Viscosity, η (mPa·s)	1.03	1.68	0.96	9.66
Velocity of sinking, ν (nm/s)	2.15	0.08	1.78	0.41
Brownian motion, d (nm)	6.75	9.54	6.75	8.24
d / ν (s)	3.14	119.25	3.79	20.10

We believe that the discrepancy between the theoretical values and the experimental data shown in Table 1 could be explained by the presence of a repulsive force between particles in the slurry. Herein, the surface electrostatic repulsive force between neighbouring particles is considered, which can be reflected by the zeta potential measurements. It is documented in the literature that when the absolute value of the zeta potential exceeds 30 mV, the particle suspension is in a stable state. As shown in Fig. 4, the absolute zeta potential values of all powders in our experiments were greater than 30 mV, indicating that all powders exerted strong repulsive forces in the slurry. Based on the aforementioned,

we concluded that the natural motion and surface charge of powders synergistically contributed to the remarkable stability of the slurries. Because each type of raw powder had the same negative charge, the heterogeneous deposition phenomenon did not occur during the fabrication of the hybrid slurries.

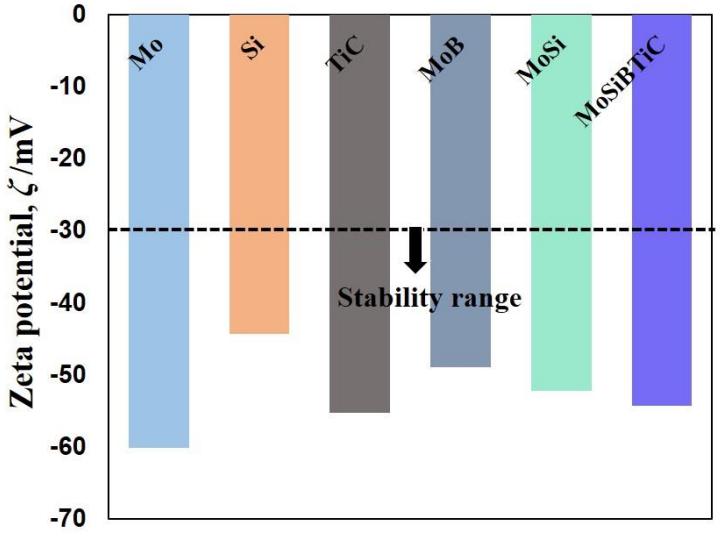

Figure 4. The zeta potential of various powders dispersed in water.

The slurry viscosity is a critical parameter required for the FD-POEM process. Thus, the viscosities of various powder slurries were investigated at room temperature. As shown in Fig. 5, the slurry viscosity exhibits a linear increasing trend with an increase in the slurry concentration. In addition, the range of slurry viscosity that is suitable for FD-POEM was determined. The dotted line in Fig. 5 indicates the viscosity limit of 50 mPa·s for the operation. When the viscosity exceeds 50 mPa·s, the slurry cannot be ejected from the orifice, regardless of the diaphragm movement.

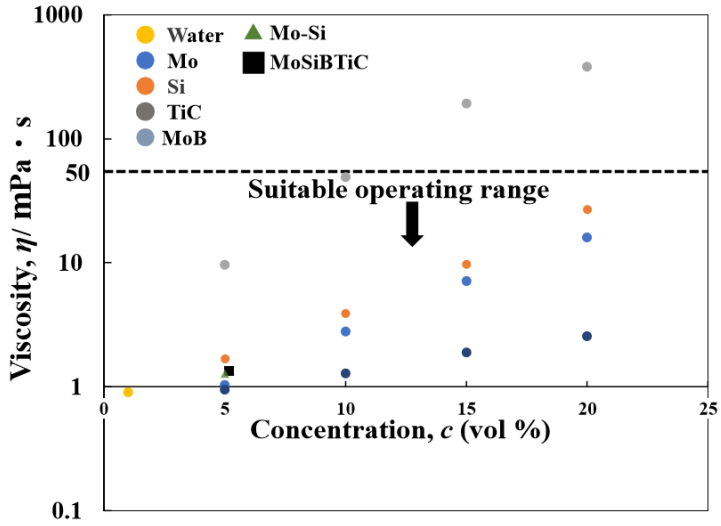

Figure 5. The slurry concentration dependent of the slurry viscosity.

3.2 Fabrication and Evaluation of FD-POEM particles

(1) Single-component FD-POEM particles

Single-component powders of Mo, Si, MoB, and TiC were fabricated individually. The typical morphologies are shown in Fig. 6. All FD-POEM particles were nearly spherical and displayed a rough surface. Many internal pores were present in the FD-POEM particles. The formation mechanism of pores is closely related to the nature of FD-POEM, which will be discussed in Section 3.3. The surface features of the various FD-POEM particles exhibit significant differences. As shown in Fig. 6, the Mo and MoB FD-POEM particles have rougher surfaces than those of the Si and TiC particles. This difference was possibly caused by the size difference of the raw powders. These FD-POEM particles are composed of raw nano or micro-sized particles. First, the small nanoparticles are prone to rearrange and stack owing to the surface tension created during the pulsated orifice ejection process. Second, the interaction between small particles is greater than that of large particles, according to the negative correlation between the van der Waals force and the size of the particles [41,42]. The Si and TiC FD-POEM particles consisting of smaller raw powders exhibited stronger cohesion forces compared to those of Mo and MoB, thereby decreasing the surface roughness.

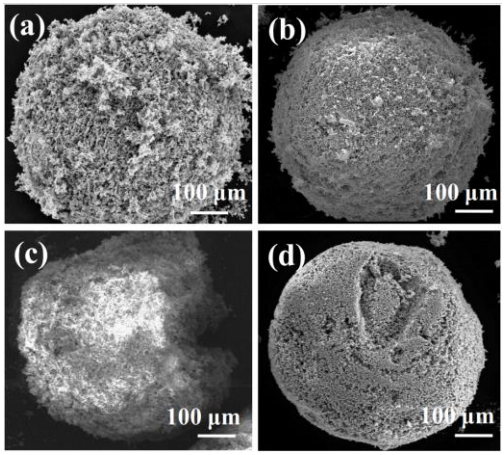

Figure 6. SEM images of the monodispersed single-component (a) Mo, (b) Si, (c) MoB, (d) TiC particles by FD-POEM.

(2) Binary-component FD-POEM particles

To verify the feasibility of preparing arbitrary-component particles by FD-POEM, Mo-Si composite particles were fabricated with various elemental ratios. Mo-10at.% Si, Mo-30at% Si, Mo-50at% Si and Mo-70at% Si composite slurries with a concentration of 5 vol.% were prepared and processed by FD-POEM, respectively. As shown in Fig. 7, as the Si content increased, the surface of the FD-POEM particles became denser and smoother. However, the sizes of the Mo-Si FD-POEM particles, d_{50}, are similar, in the range of 730 - 780µm. This indicates that the composition and concentration of the slurry have an insignificant influence on the particle size of the FD-POEM particles. Therefore, spherical FD-POEM particles with arbitrary composition ratios can be prepared by FD-POEM.

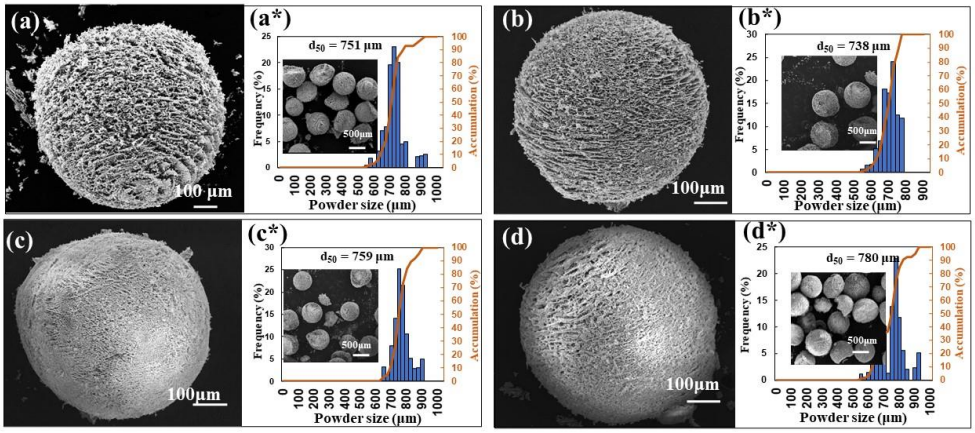

Figure 7. The SEM images and size distribution of the FD-POEM particles (a: Mo-10at%Si; b: Mo-30at%Si; c: Mo-50at%Si; d: Mo-70at%Si). The inserts were low-magnification microphotographs.

(3) Multicomponent FD-POEM particles

A spherical multi-component particle of MoSiMoTiC was also prepared (see Fig. 8a). As confirmed by SEM-EDS mappings, elemental Mo, Si, and Ti were evenly distributed on the particle surface. Fig. 8(f) shows the particle size distribution of the MoSiBTiC particles fabricated by FD-POEM. It can be seen that the size distribution is within a narrow range and follows a typical Gaussian curve. The particle size d_{50} was determined to be 745 µm.

In addition, the powder flowability of FD-POEM particles was reflected by a revolution method, where lower avalanche angles indicated better flowability. The avalanche angle of the FD-POEM MoSiBTiC particles was measured to be 42.6°, which is lower than that of the ball-milled alloy powders (~50.5°). This improvement in flowability was attributed to the spherical shape of the FD-POEM particles. Notably, this is the first time that refractory composite particles were fabricated directly without a melting process.

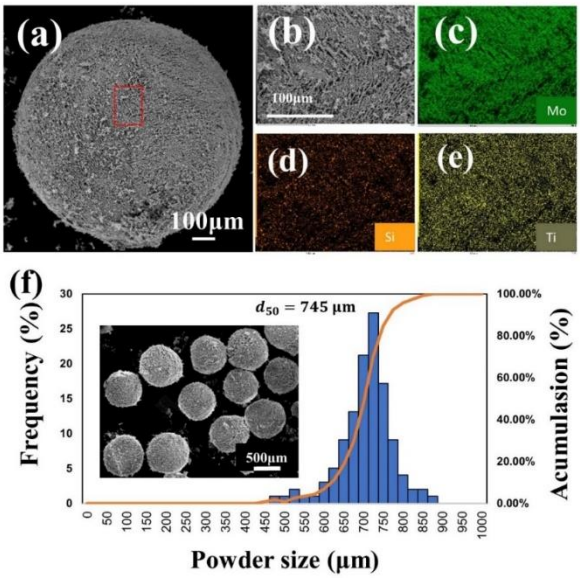

Figure 8. (a) SEM images of Mo-Si-MoB-TiC particles by FD-POEM; (b, c, d, e) The enlarged area marked in red box in (a) and corresponding EDS mappings; (f) The size distribution and low-magnification SEM image of Mo-Si-MoB-TiC particles.

3.3 Formation mechanism of pores in FD-POEM particles

To investigate the internal structure of the FD-POEM particles, we performed high-magnification observations using a field emission scanning electron microscope (FE-SEM). Figs. 9(a) and (b) show low and high magnifications, respectively of an FD-POEM Mo-30at.% Si particle. This particle showed porous structures with flaky topography. The porous feature was further confirmed by cross-sectional X-ray CT as shown in Figs. 9(c-d) taken from the red line in Fig. 9a. It is noted that the micro-sized voids with radial dendrites (green arrow in Fig. 9d) extend from the outside to the inside. Moreover, some smaller voids were observed in the central area of the particle (yellow arrow in Fig. 9d). These voids were formed during the freezing and drying processes. Once the slurry encounters liquid nitrogen, ice crystallization starts driven by a temperature gradient. The raw powders were rejected by the ice crystal growth and concentrated between the ice crystals, as illustrated in Fig. 10a.

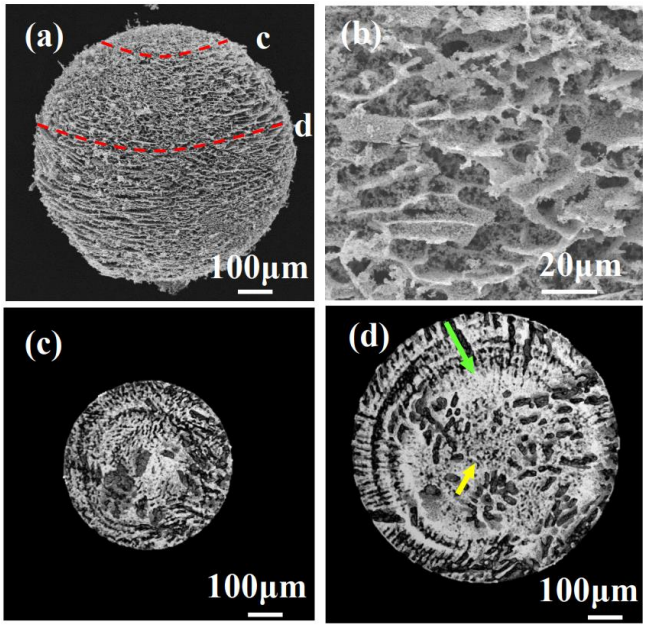

Figure 9. (a)low-magnification and (b) high-magnification SEM images of a Mo-30at%Si FD-POEM particle. (c, d) the X-ray CT images of the areas marked by red lines in (a).

The distribution and movement of nanopowders in the ice crystals were influenced by thermodynamics during crystallization resulting in the formation of voids. Subsequently, the ice crystals containing nanoparticles were exposed to the continuous cooling. The pores were generated further from the sublimation of the ice crystals, leading to the radial distribution of voids from the outside to the inside of the particle (Fig 10b). Therefore, the spherical FD-POEM particles exhibited a mesh-pored structure following the track of the sublimated ice crystals.

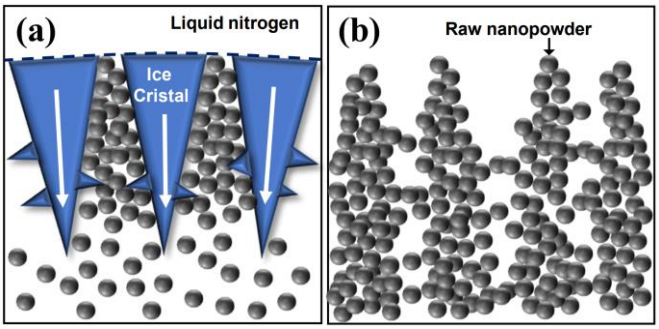

Figure 10. (a) Schematic diagrams of (a) ice crystal growth during the freezing process and (b) ice sublimation during the freeze-drying process. The white arrows in (a) indicate the direction of ice crystal growth.

In general, the porosity p is a parameter used to evaluate the quality of particles. Here, the porosity value of the FD-POEM particles can be calculated based on Equation 4:

$$p = 1 - \frac{\frac{\omega_1 \times m}{\rho_1} + \frac{\omega_2 \times m}{\rho_2} + \cdots + \frac{\omega_i \times m}{\rho_i}}{V} \quad (4)$$

where ω_i, ρ are the mass fraction and density of component i, respectively. m and V are the weight and volume of an FD-POEM particle, respectively. Correspondingly, the actual porosity was calculated to be 93.2±5 vol.%. This value is consistent with the water volume fraction in the 95 vol.%. In contrast, the porosity was measured to be ~14.0 vol% from the X-ray CT analysis in Figs. 9(c-d), which is much lower than the actual value, attributed to the limited resolution of X-ray CT (~ 3.1μm). This result indicates that ~80% of the pores in the PD-POEM particles have a small size (< 3.1 μm).

Because L-PBF requires a powder size smaller than 100 μm, the FD-POEM particles fabricated in our study cannot be used directly for L-PBF. However, in the near future, our main work will focus on the control of FD-POEM particle size by adjusting the pipe orifice size and vibration movement of the diaphragm. The microstructure and mechanical performance of L-PBF parts using FD-POEM particles will also investigated.

4 Conclusion

In this study, a novel powder preparation method, FD-POEM, was systematically developed to fabricate refractory alloy composite particles. The main conclusions are summarized as follows:

(1) High-concentration, stable slurries were prepared by dispersing submicron Mo, Si, MoB, and TiC powders in water. It was found that the viscosity of the slurry should be lower than 50 mPa·s to meet the operating requirements of FD-POEM.

(2) Spherical composite particles with arbitrary composition ratios could be fabricated by FD-POEM. The particles had a narrow size range and uniform elemental distribution. Moreover, many mesh pores ~ 93.2% in volume were formed within the FD-POEM fabricated particles, which was attributed to the ice crystal freezing process and subsequent ice sublimation.

(3) Owing to their spherical morphology, the FD-POEM particles had a low avalanche angle of 42.6°, exhibiting good flowability. This study offers new insights into the production of complex system refractory particles, such as MoSiBTiC alloy particles and high-entropy alloy particles for L-PBF.

References

1 Perepezko, J. H. The hotter the engine, the better. *Science* **326**, 1068-1069 (2009).

2 Senkov, O. *et al.* Microstructure and elevated temperature properties of a refractory TaNbHfZrTi alloy. *Journal of Materials Science* **47**, 4062-4074 (2012).

3 Kamata, S. Y. *et al.* Ultrahigh-temperature tensile creep of TiC-reinforced Mo-Si-B-based alloy. *Scientific reports* **8**, 10487 (2018).

4 Dimiduk, D. M. & Perepezko, J. H. Mo-Si-B alloys: developing a revolutionary turbine-engine material. *Mrs Bulletin* **28**, 639-645 (2003).

5 Lemberg, J. A. & Ritchie, R. O. Mo‐Si‐B Alloys for Ultrahigh‐Temperature Structural Applications. *Advanced Materials* **24**, 3445-3480 (2012).

6 Yoshimi, K. *et al.* High-temperature compressive properties of TiC-added Mo-Si-B alloys. *JOM* **66**, 1930-1938 (2014).

7 Nakamura, J., Kanekon, D. & Yoshimi, K. Characterization of Mo/Mo2C interface in MoSiBTiC alloy. *Materials Letters* **180**, 340-343 (2016).

8 Moriyama, T. *et al.* Room-temperature fracture toughness of MoSiBTiC alloys. *Intermetallics* **84**, 92-102 (2017).

9 Uemura, S. *et al.* Quantitative evaluation of microstructure in Mo-Si-B-TiC alloy produced by melting and tilt casting methods. *Materials Transactions* **59**, 136-145 (2018).

10 Kamata, S. Y. *et al.* Ultrahigh-temperature tensile creep of TiC-reinforced Mo-Si-B-based alloy. *Scientific reports* **8**, 1-14 (2018).

11 Fukuyama, H., Sawada, R., Nakashima, H., Ohtsuka, M. & Yoshimi, K. Study of solidification pathway of a MoSiBTiC alloy by optical thermal analysis and in-situ observation with electromagnetic levitation. *Scientific Reports* **9**, 1-11 (2019).

12 Jéhanno, P., Heilmaier, M. & Kestler, H. Characterization of an industrially processed Mo-based silicide alloy. *Intermetallics* **12**, 1005-1009 (2004).

13 Jéhanno, P. *et al.* Molybdenum alloys for high temperature applications in air. *Powder Metallurgy* **51**, 99-102 (2008).

14 Zhou, W. *et al.* Powder fabrication and laser additive manufacturing of MoSiBTiC alloy. *Intermetallics* **104**, 33-42 (2019).

15 Abe, F., Osakada, K., Shiomi, M., Uematsu, K. & Matsumoto, M. The manufacturing of hard tools from metallic powders by selective laser melting. *Journal of materials processing technology* **111**, 210-213 (2001).

16 Kruth, J.-P. *et al.* Selective laser melting of iron-based powder. *Journal of materials processing technology* **149**, 616-622 (2004).

17 Thijs, L., Verhaeghe, F., Craeghs, T., Van Humbeeck, J. & Kruth, J.-P. A study of the microstructural evolution during selective laser melting of Ti–6Al–4V. *Acta materialia* **58**, 3303-3312 (2010).

18 Karlsson, J., Snis, A., Engqvist, H. & Lausmaa, J. Characterization and comparison of materials produced by Electron Beam Melting (EBM) of two different Ti–6Al–4V powder fractions. *Journal of materials processing technology* **213**, 2109-2118 (2013).

19 Zhao, X., Chen, J., Lin, X. & Huang, W. Study on microstructure and mechanical properties of laser rapid forming Inconel 718. *Materials Science and Engineering: A* **478**, 119-124 (2008).

20 Ali, U. *et al.* On the measurement of relative powder-bed compaction density in powder-bed additive manufacturing processes. *Materials & Design* **155**, 495-501 (2018).

21 Sutton, A. T., Kriewall, C. S., Leu, M. C. & Newkirk, J. W. Powder characterisation techniques and effects of powder characteristics on part properties in powder-bed fusion processes. *Virtual and physical prototyping* **12**, 3-29 (2017).

22 Sayedain, S. S., Ekrami, A. & Badrossamay, M. Production and characterization of Ti6Al4V/CaP nanocomposite powder for powder-based additive manufacturing systems. *Powder Technology* (2021).

23 Olakanmi, E. O., Cochrane, R. & Dalgarno, K. A review on selective laser sintering/melting (SLS/SLM) of aluminium alloy powders: Processing, microstructure, and properties. *Progress in Materials Science* **74**, 401-477 (2015).

24 Zhou, W. *et al.* Carbon nanotubes as a unique agent to fabricate nanoceramic/metal composite powders for additive manufacturing. *Materials & Design* **137**, 276-285, doi:https://doi.org/10.1016/j.matdes.2017.10.034 (2018).

25 Li, Y. & Gu, D. Parametric analysis of thermal behavior during selective laser melting additive manufacturing of aluminum alloy powder. *Materials & Design* **63**, 856-867 (2014).

26 Vilaro, T., Colin, C., Bartout, J.-D., Nazé, L. & Sennour, M. Microstructural and mechanical approaches of the selective laser melting process applied to a nickel-base superalloy. *Materials Science and Engineering: A* **534**, 446-451 (2012).

27 Song, B., Dong, S., Deng, S., Liao, H. & Coddet, C. Microstructure and tensile properties of iron parts fabricated by selective laser melting. *Optics & Laser Technology* **56**, 451-460 (2014).

28 Fereiduni, E., Ghasemi, A. & Elbestawi, M. Characterization of composite powder feedstock from powder bed fusion additive manufacturing perspective. *Materials* **12**, 3673 (2019).

29 Zhou, W., Tsunoda, K., Nomura, N. & Yoshimi, K. Effect of hot isostatic pressing on the microstructure and fracture toughness of laser additive-manufactured MoSiBTiC multiphase alloy. *Materials & Design* **196**, 109132 (2020).

30 Sun, P., Fang, Z. Z., Zhang, Y. & Xia, Y. Review of the methods for production of spherical Ti and Ti alloy powder. *Jom* **69**, 1853-1860 (2017).

31 McCracken, C. G., Motchenbacher, C. & Barbis, D. P. REVIEW OF TITANIUM-POWDER-PRODUCTION METHODS. *International journal of powder metallurgy* **46** (2010).

32 Roberts, P. The production of PREP titanium powder. *Metal Powder Industries Federation*, 427-438 (1989).

33 Sun, P., Fang, Z. Z., Xia, Y., Zhang, Y. & Zhou, C. A novel method for production of spherical Ti-6Al-4V powder for additive manufacturing. *Powder Technology* **301**, 331-335 (2016).

34 Nie, Y., Tang, J., Huang, J., Yu, S. & Li, Y. A Study on Internal Defects of PREP Metallic Powders by Using X-ray Computed Tomography. *Materials* **14**, 1177 (2021).

35 Boulos, M. Plasma power can make better powders. *Metal Powder Report* **59**, 16-21 (2004).

36 Higashi, M. & Ozaki, T. Selective laser melting of MoSiBTiC alloy with plasma-spheroidized powder: Microstructure and mechanical property. *Materials Characterization* **172**, 110888 (2021).

37 Upadhyay, R. K. & Kumar, A. Boundary lubrication properties and contact mechanism of carbon/MoS2 based nanolubricants under steel/steel contact. *Colloid and Interface Science Communications* **31**, 100186 (2019).

38 Simha, R. The Influence of Brownian Movement on the Viscosity of Solutions. *The Journal of physical chemistry* **44**, 25-34 (1940).
39 Felderhof, B. & Jones, R. Linear response theory of the viscosity of suspensions of spherical brownian particles. *Physica A: Statistical Mechanics and its Applications* **146**, 417-432 (1987).
40 Dhont, J. K. *An introduction to dynamics of colloids*. (Elsevier, 1996).
41 Parteli, E. J. *et al.* Attractive particle interaction forces and packing density of fine glass powders. *Scientific reports* **4**, 1-7 (2014).
42 Chen, H., Wei, Q., Wen, S., Li, Z. & Shi, Y. Flow behavior of powder particles in layering process of selective laser melting: Numerical modeling and experimental verification based on discrete element method. *International Journal of Machine Tools and Manufacture* **123**, 146-159 (2017).

Acknowledgement

This research was partially supported by the JST-MIRAI Program, Grant Number JPMJMI17E7 in Japan.

Author information

Affiliations

Department of Materials Processing, Graduate School of Engineering, Tohoku University, Sendai, Miyagi, 980-8579, Japan

Zhenxing Zhou, Suxia Guo, Weiwei Zhou & Naoyoki Nomura

Contributions

Zhenxing Zhou contributed on designing the experiment, performing the fabrication and analysing the results. Suxia Guo and Weiwei Zhou analysed the results. Naoyoki Nomura supervised the research.

Corresponding author

Correspondence to Weiwei Zhou & Naoyoki Nomura.

Ethics declarations

Competing interests

The authors declare no competing interests.

Figures

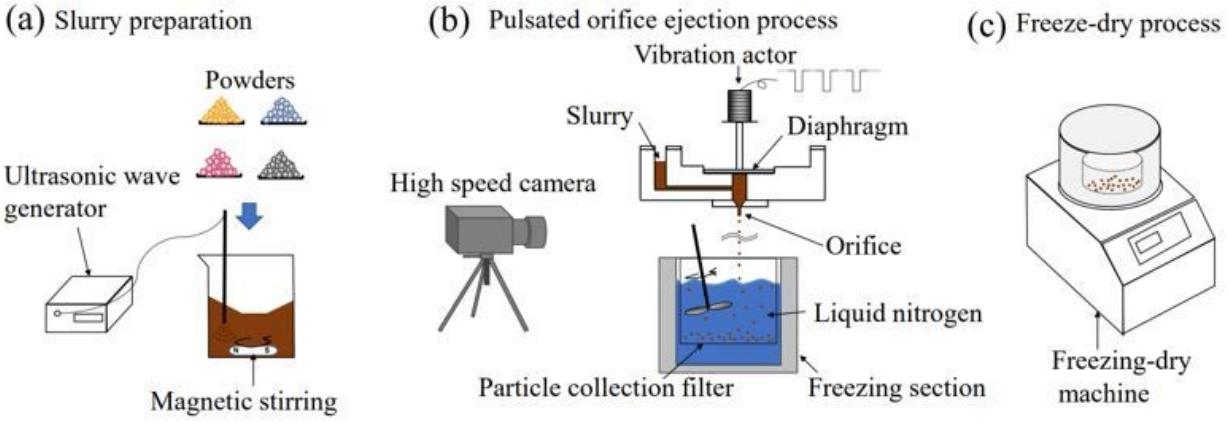

Figure 1

Schematic diagram of FD-POEM process: (a) Fabrication process of the slurry; (b) Preparation of composite particles by pulsated orifice ejection method; (c) Freeze-drying process.

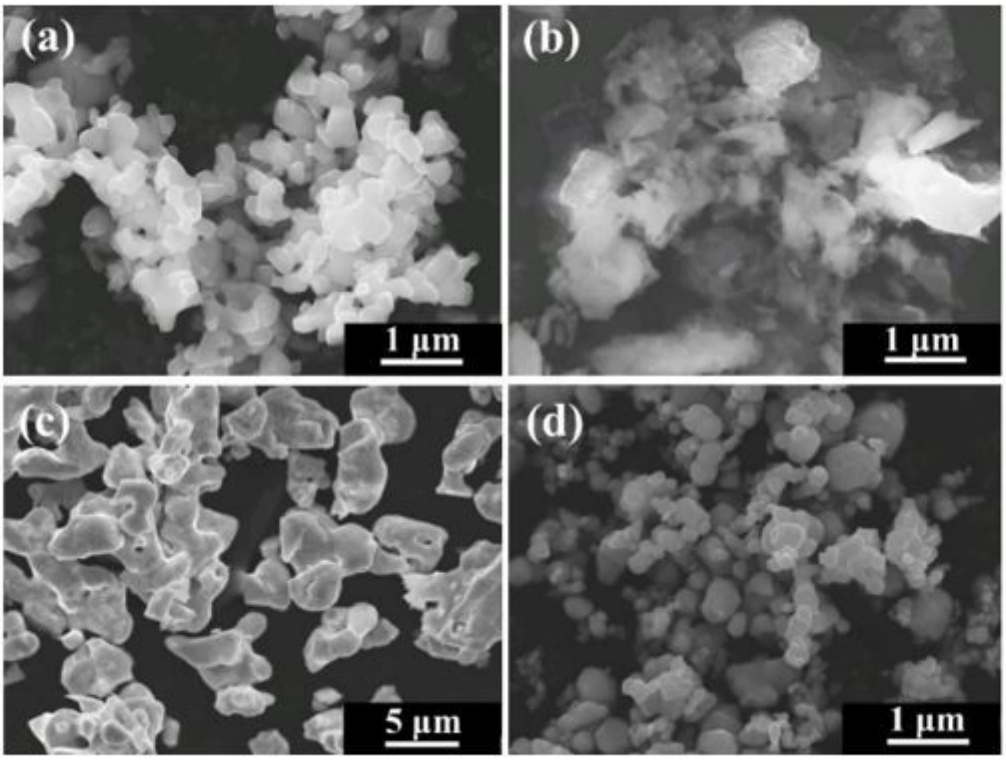

Figure 2

SEM images of the raw (a) Mo, (b)Si, (c) MoB, and (d)TiC powders.

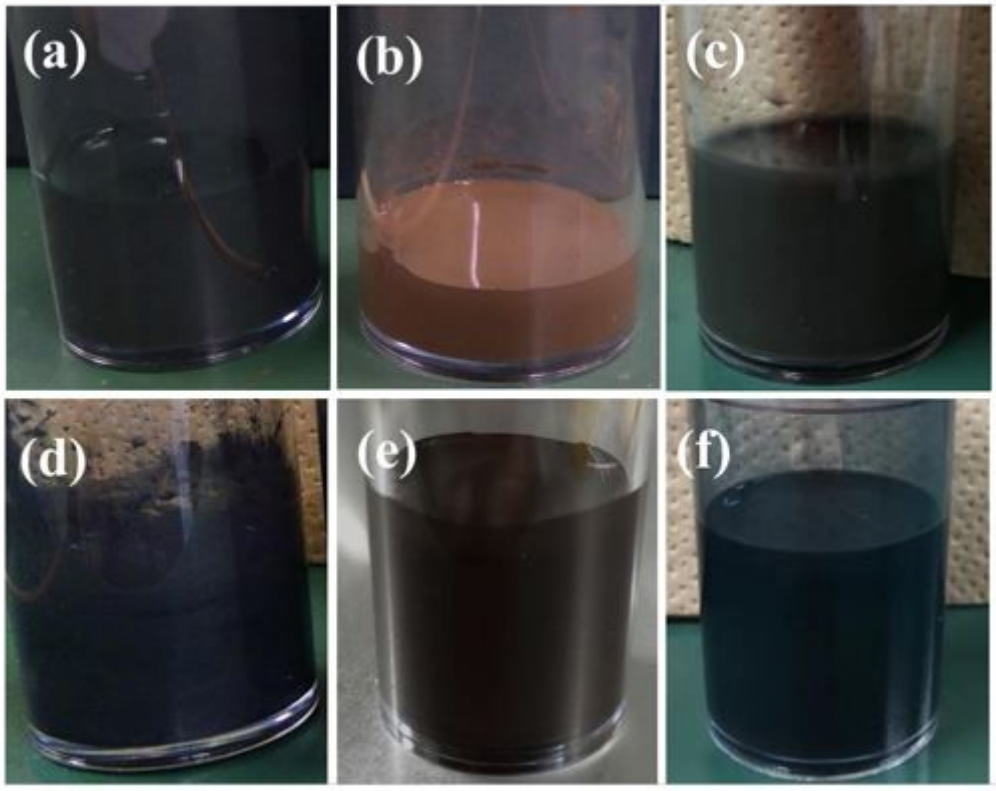

Figure 3

The appearance of 5 vol. % (a) Mo, (b) Si, (c)MoB, (d)TiC, (e)Mo-Si, (f)Mo-Si-MoB-TiC slurries.

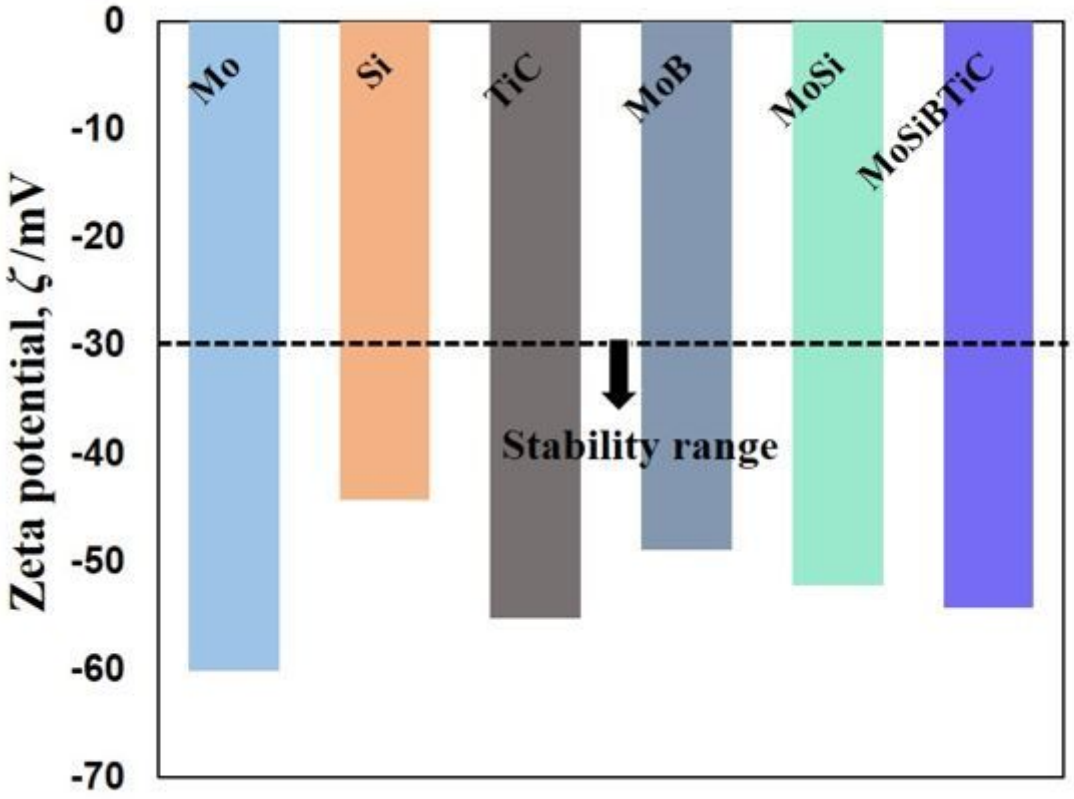

Figure 4

The zeta potential of various powders dispersed in water.

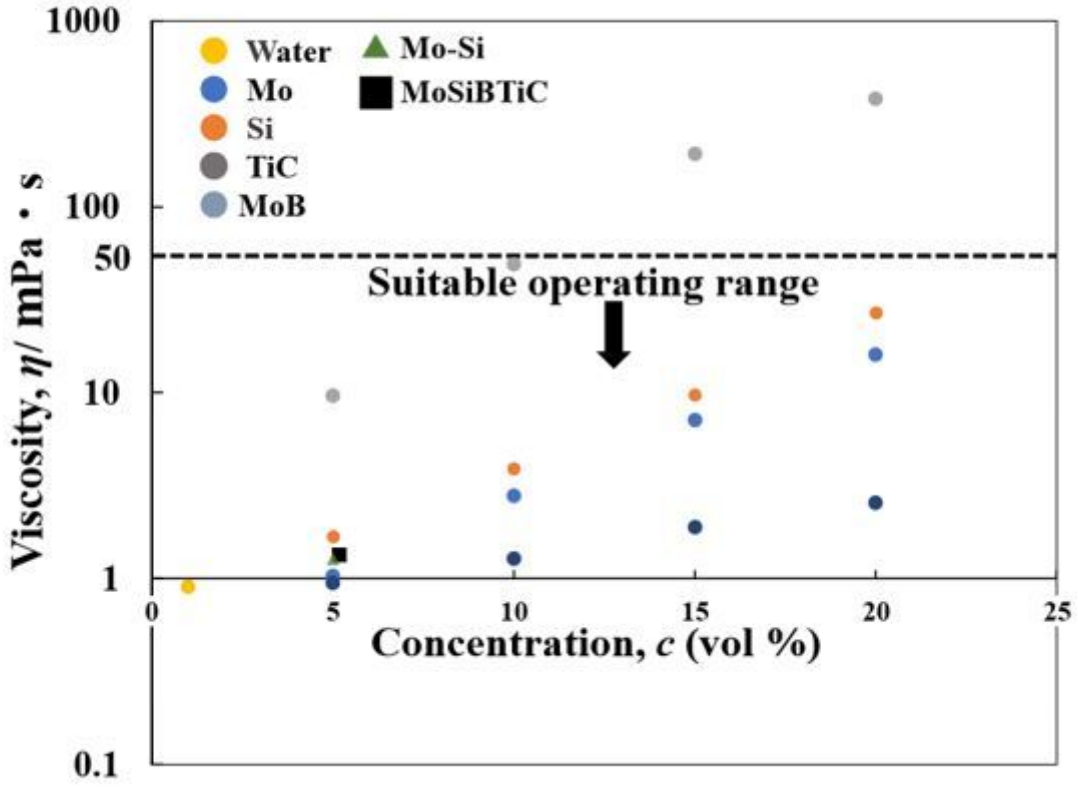

Figure 5

The slurry concentration dependent of the slurry viscosity.

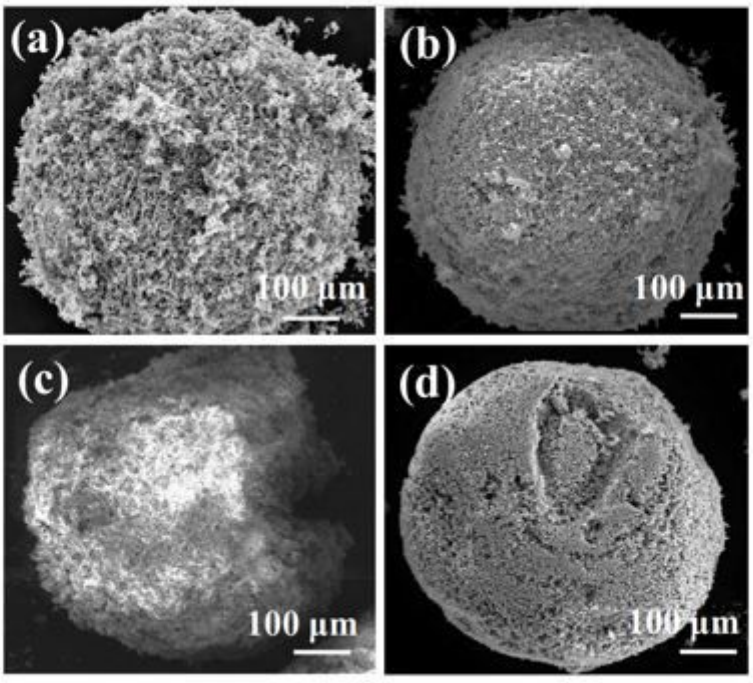

Figure 6

SEM images of the monodispersed single-component (a) Mo, (b) Si, (c) MoB, (d) TiC particles by FD-POEM.

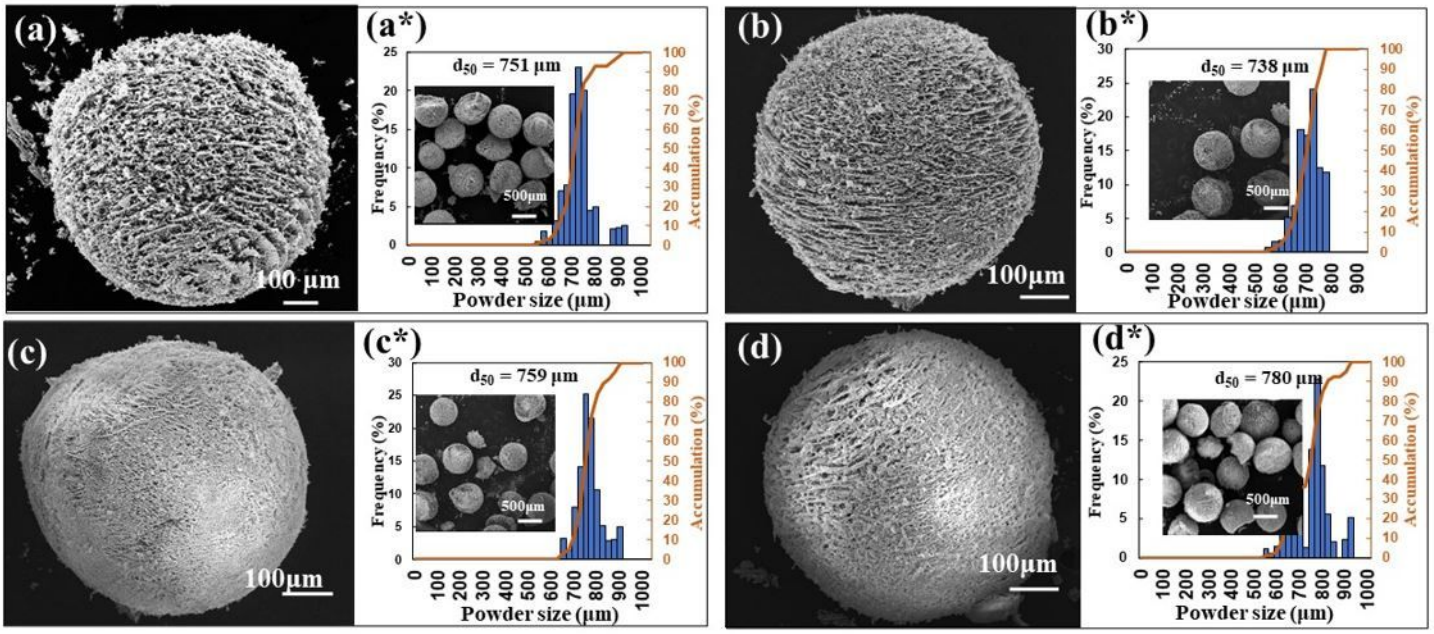

Figure 7

The SEM images and size distribution of the FD-POEM particles (a: Mo-10at%Si; b: Mo-30at%Si; c: Mo-50at%Si; d: Mo-70at%Si). The inserts were low-magnification microphotographs.

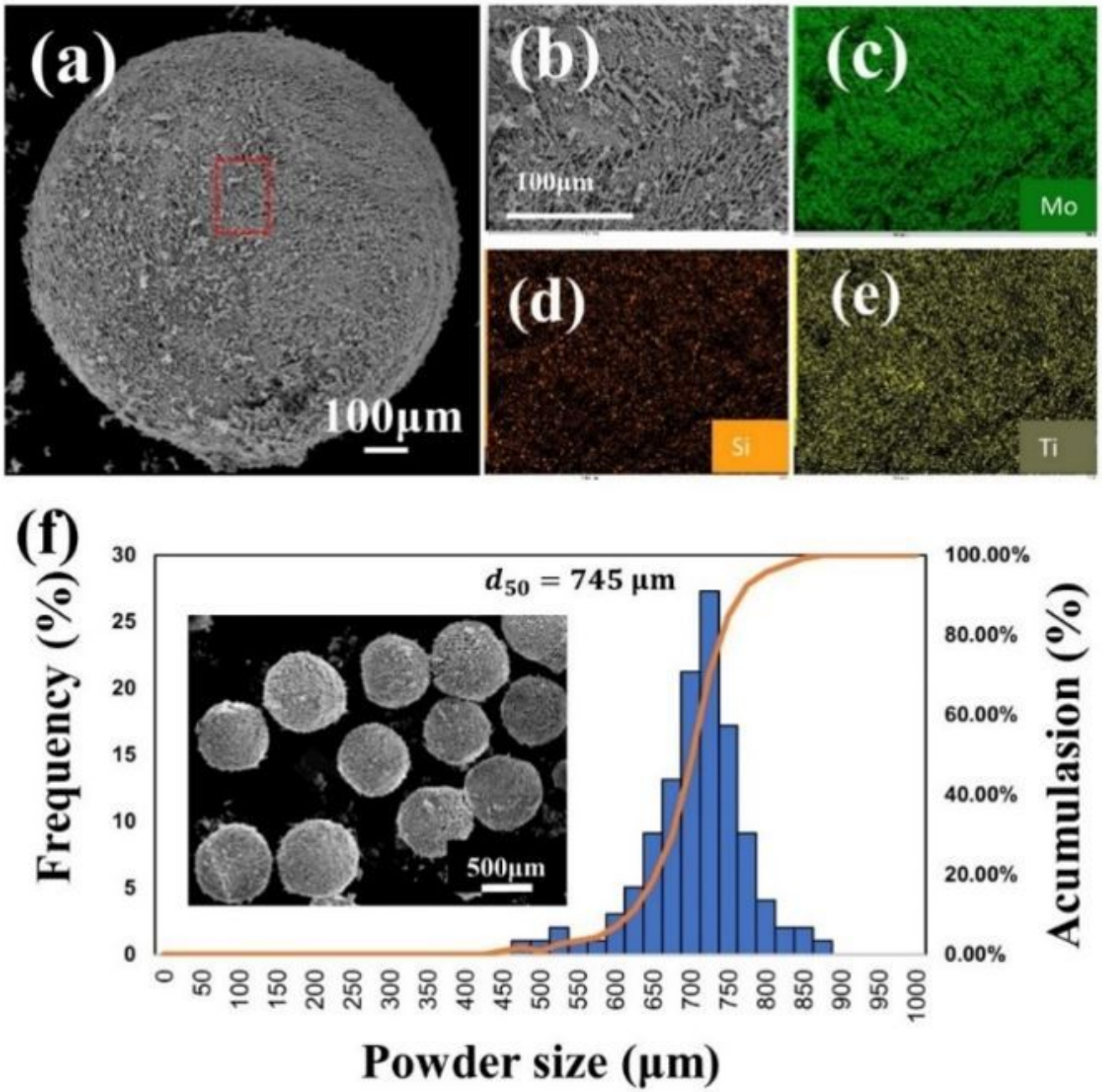

Figure 8

(a) SEM images of Mo-Si-MoB-TiC particles by FD-POEM; (b, c, d, e) The enlarged area marked in red box in (a) and corresponding EDS mappings; (f) The size distribution and low-magnification SEM image of Mo-Si-MoB-TiC particles.

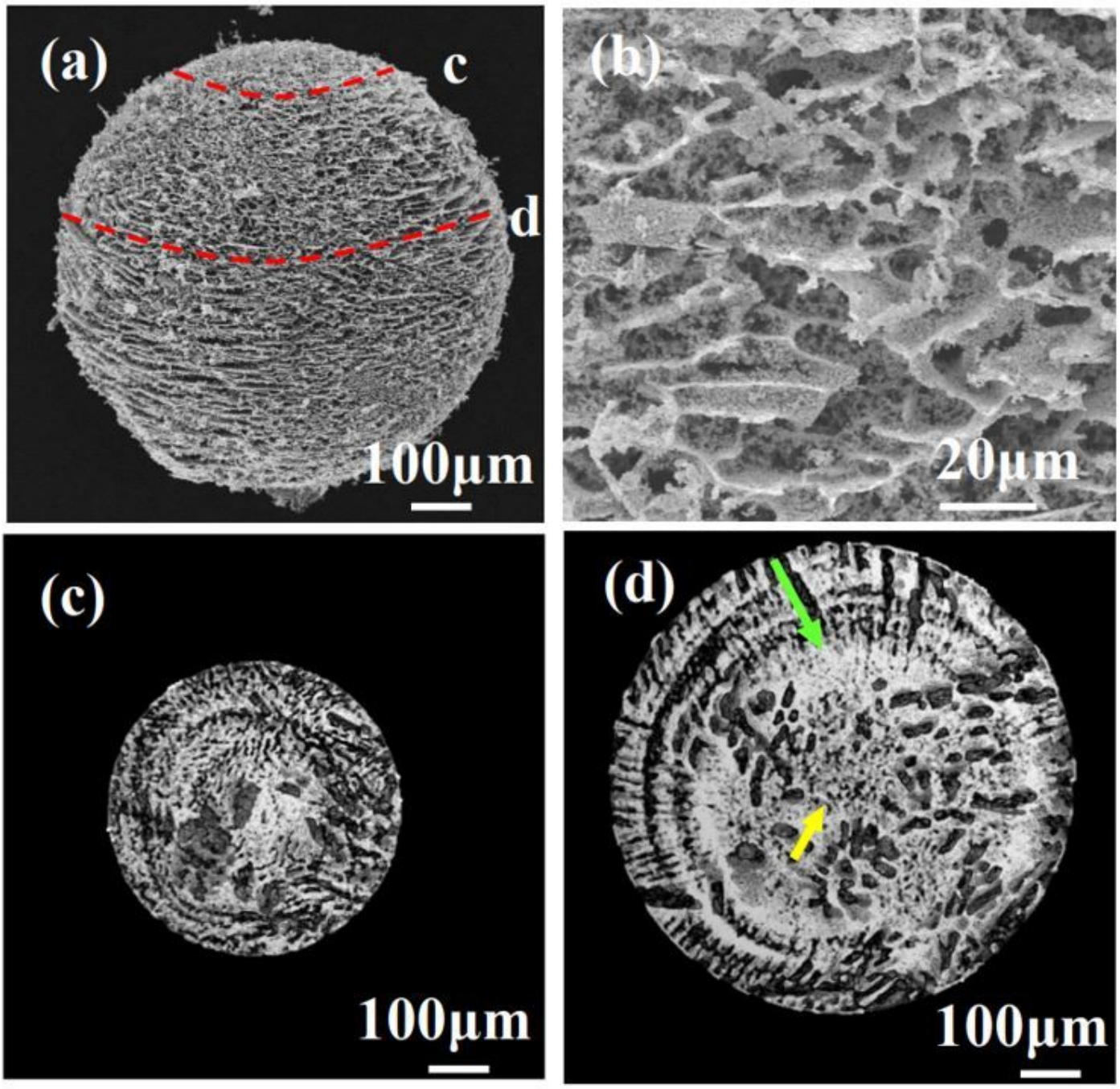

Figure 9

(a)low-magnification and (b) high-magnification SEM images of a Mo-30at%Si FD-POEM particle. (c, d) the X-ray CT images of the areas marked by red lines in (a).

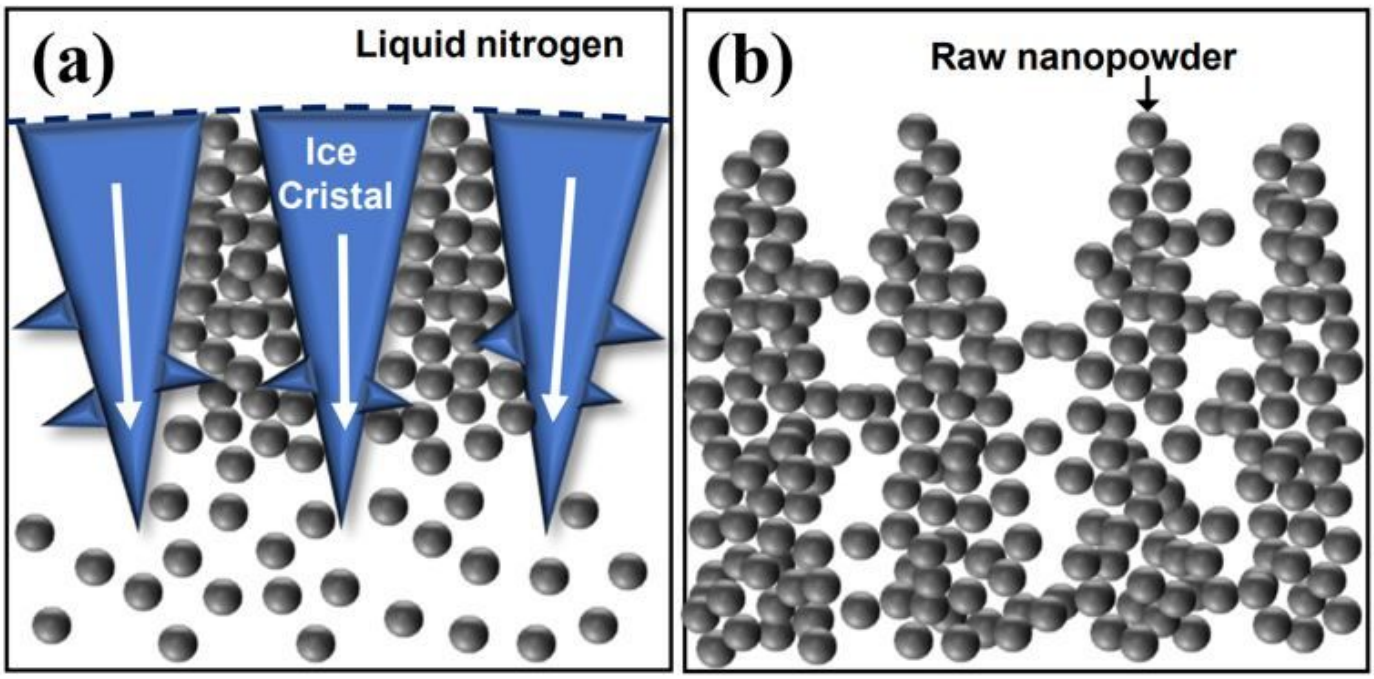

Figure 10

(a) Schematic diagrams of (a) ice crystal growth during the freezing process and (b) ice sublimation during the freeze-drying process. The white arrows in (a) indicate the direction of ice crystal growth.